

NUMERICAL STUDY OF THE INTERNAL WAVE BEHAVIOUR IN THE VERTICAL OCEAN SLICE MODEL

SYAMSUL RIZAL^{1,2,*}, TAUFIQ ISKANDAR³,
MUHAMMAD¹, YUDI HADITIAH², YOPI ILHAMSYAH¹,
ICHSAN SETIAWAN^{1,2}, HIZIR SOFYAN⁴

¹Department of Marine Sciences, Faculty of Marine and Fisheries,
Universitas Syiah Kuala, Banda Aceh 23111, Indonesia

²Graduate School of Mathematics and Applied Sciences, Universitas Syiah Kuala,
Banda Aceh 23111, Indonesia

³Department of Mathematics, Faculty of Mathematics and Natural Sciences,
Universitas Syiah Kuala, Banda Aceh 23111, Indonesia

⁴Department of Statistics, Faculty of Mathematics and Natural Sciences,
Universitas Syiah Kuala, Banda Aceh 23111, Indonesia

*Corresponding Author: syamsul.rizal.unsyiah.net

Abstract

Internal waves can occur in the ocean and in the atmosphere. They contribute greatly to the ecosystem and climate change. Although the amplitude of internal waves within the ocean is very large, the effects of internal waves are very difficult to detect at sea level. The motivation of this article is to study the characteristics of internal waves. We use two-dimensional numerical methods in horizontal and vertical directions. In these numerical experiments, we set up the internal waves in the channel with length and width of 500 m and 100 m, respectively. This model has a resolution 5 m and 2 m in the horizontal and vertical direction, respectively. The density is added 10 kg/m^3 linearly with 10 m depth, while at the surface the density remains constant at 1028 kg/m^3 . In order to drive the density disturbances in the channel, in the middle of the channel (5 grid cells), the density of 20 kg/m^3 is added for each layer. The result shows that the signal of internal wave time-series is varied in terms of amplitudes and periods. The minimum period is 62.8 s, and it is consistent with the theory.

Keywords: Density, Internal waves, Numerical simulation, Period, Stability frequency.

1. Introduction

The internal wave has a little effect on the surface water. The influences on sea-level can be ignored, generating a gain of about 1-2 cm and almost invisible in the turbulent sea [1]. But internal waves, which are hidden completely in the sea, their amplitudes in the sea can reach more than 100 meters [2-4] and has a profound effect on earth's climate and marine ecosystem [5-7]. In the cross-sectional view, the internal waves take the same form as surface waves. The only difference of the water mass movement between the underwater and surface water waves is the density [8, 9].

Research on the internal waves is still rarely performed. Since the internal wave occurred below the sea surface, its behaviour is difficult to detect [10]. The influences of the internal wave to the sea-surface are minimal, just a few centimeters. As a result, in a turbulent sea, internal wave effect on the sea-surface is almost undetectable.

In contrast to research on sea-surface, the internal waves are not visible to the eye. This is one of the reasons, why the study of internal waves are still very rare as previously stated, despite these internal waves as mentioned earlier have greatly affected on marine ecosystems and climate of our planet.

Besides, internal waves also affect the transport of suspended particulate matter, larval transport [11], and turbulent dissipation as well as diapycnal mixing [12]. Studying internal waves is also useful in engineering and industrial applications. Menni et al. [13-15] and Menni and Azzi [16] studied fluid flow and heat transfer with various baffle.

From a fundamental and practical standpoint, internal waves in the stratified ocean are very important and have significant implications for many physical and biological processes [17].

Several types of research of internal waves have been done to investigate its physical characteristics, e.g., Mercier et al. [18], Shanmugam [19] and Cheriton et al. [20]. Based on the above statements, it can be said that internal wave phenomena are very important to be investigated. Thus, the research on modeling is essential to perform to investigate the behaviour of hidden internal wave in the deep layer as studies by Matthews et al. [21] and Salloum et al. [22]. In the present research, numerical experiments are conducted to investigate the response of internal wave on density variation in a finite channel. The specific objective of this study is to understand the behaviour of internal waves in details.

2. Procedures

The model is driven by the following equations of motion in u and w -direction [23]:

$$\frac{\partial u}{\partial t} = -\frac{1}{\rho_0} \frac{\partial P}{\partial x} \quad (1)$$

$$\frac{\partial w}{\partial t} = -\frac{1}{\rho_0} \frac{\partial P}{\partial z} - \frac{\rho'}{\rho_0} g \quad (2)$$

$$\frac{\partial u}{\partial x} + \frac{\partial w}{\partial z} = 0 \quad (3)$$

$$\frac{\partial \rho}{\partial t} + w \frac{\partial \bar{\rho}}{\partial z} = 0 \quad (4)$$

It is assumed that in Eq. (4), term $\frac{\partial \bar{\rho}}{\partial z}$ has a vertical variation of density. This term related to a stability frequency of $N^2 = (-g/\rho_0)\partial \bar{\rho}/\partial z$. This is a non-hydrostatic model. It is different from the hydrostatic model that was previously used [24-27].

The channel and initial condition used in this research are shown in Fig. 1. This channel is a closed-boundaries model, which covers 500 m and 100 m in length and depth, respectively. Model is run with the following initial data, $N = 0.1 \text{ s}^{-1}$ or $N^2 = 10^{-2} \text{ s}^{-2}$ and $\rho_0 = 1028 \text{ kg/m}^3$. The topography is constant. As experiments, we set a disturbance by varying the density in the middle of xz -plane as presented in Fig. 1 as the initial condition. Kampf [23] described in detail the numerical experiments, in which, were carried out numerically by the finite-difference method.

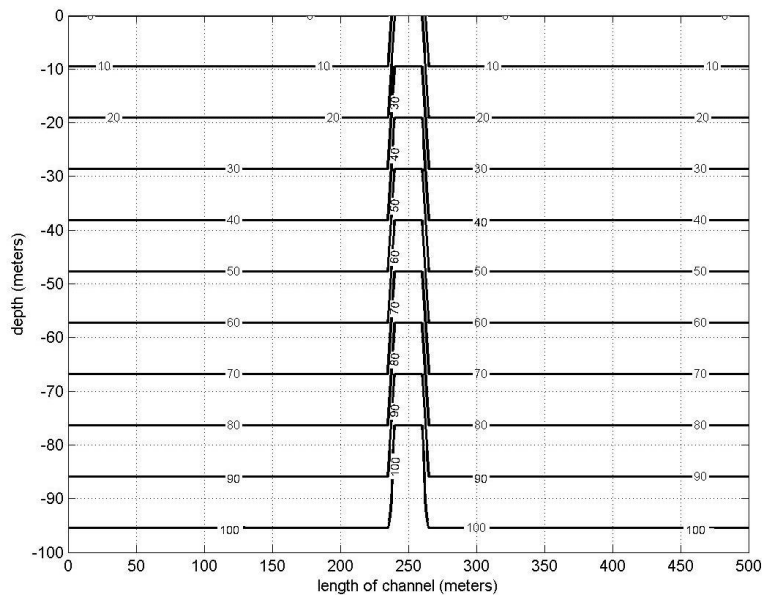


Fig. 1. The initial condition of densities for each layer. The label of contour shows $(\rho - \rho_0)$ in kg/m^3 , where $\rho_0 = 1028 \text{ kg/m}^3$. In the horizontal direction, there are 101 grid points, with $\Delta x = 5$ meters, while in the vertical direction, there are 51 grid points, with $\Delta z = 2$ meters. Except in the middle, the densities are generated with $N^2 = 10^{-2}$. To force the domain with the internal waves, in the middle channel ($x = 240 \text{ m}$ until $x = 260 \text{ m}$), the densities are set to increase 20 kg/m^3 for each layer.

3. Results and Discussions

Figure 2 shows the time-series of $(\rho - \rho_0)$ in kg/m^3 at $x = 100$ and the depth of 24, 50 and 76 m. The values of $(\rho - \rho_0)$ increase with the depth. All of 3 simulation signals have 12 crests. It can be seen also that three signals of $(\rho - \rho_0)$ time-series for each depth have peaks and troughs nearly at the same time. It means that these 3 signals have relatively the same period.

Figure 3 shows the time-series of $(\rho - \rho_0)$ in kg/m^3 at $x = 200$ and the depth of 24, 50 and 76 m. Like Fig. 2, the values of $(\rho - \rho_0)$ increase with the depth.

Different from Fig. 2, all of 3 simulation signals of Fig. 3 have 14 crests. It means, compared to time-series at $x = 100$, the signals of time-series at $x = 200$ has a smaller average period. We can also observe from Fig. 3 that three signals for each depth have crests and troughs nearly at the same time. It means that these three signals have relatively the same period.

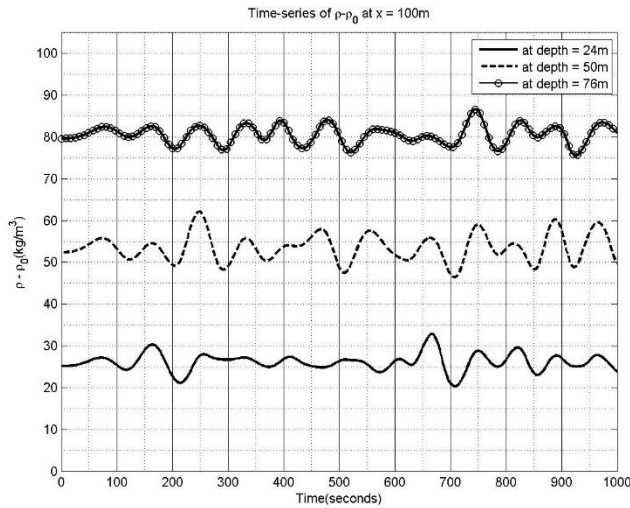


Fig. 2. Time-series of $(\rho - \rho_0)$ in kg/m^3 at $x = 100$ m and the depth of 24, 50 and 76 m.

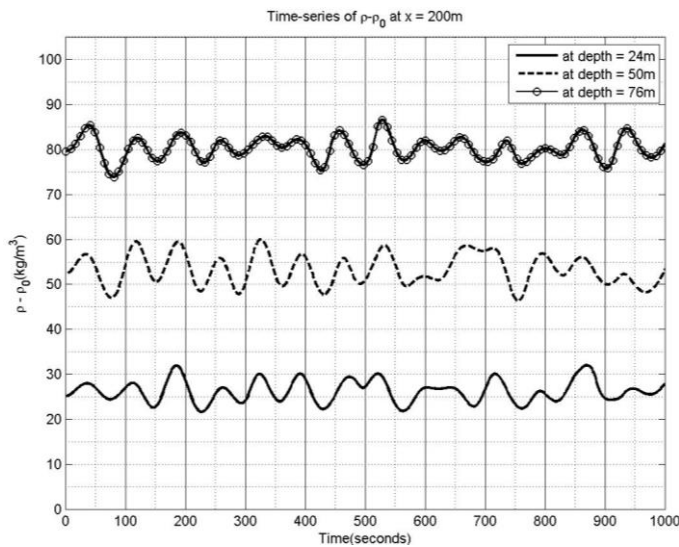


Fig. 3. Time-series of $(\rho - \rho_0)$ in kg/m^3 at $x = 200$ and the depth of 24, 50 and 76 m. The values of $(\rho - \rho_0)$ increase with the depth.

To analyse the relationship between $(\rho - \rho_0)$ and vertical velocity w , we plot deviation of $(\rho - \rho_0)$ from its mean value. By plotting this deviation, we can directly compare between $(\rho - \rho_0)$ and vertical velocity w , since both of lines are now symmetry with respect to the x -axis. The deviation of $(\rho - \rho_0)$ from its mean value is defined using the following expression:

$$\text{dev}(\rho - \rho_0) = (\rho - \rho_0) - \text{mean}(\rho - \rho_0) \quad (5)$$

Figure 4 reports the time-series of $\text{dev}(\rho - \rho_0)$ in kg/m^3 (continuous line) and time-series of vertical velocity w in cm/s (dashed line). There are 1000 points of time-simulation data for each line.

Figure 4 also shows that both of lines have 12 crests within 1000 s of time simulation. It means they have average periods of $1000/12 = 83.3$ s. According to the theory by Pond and Pickard [28], the minimum period $T_{\min} = 2\pi/N$. Therefore, the minimum period = 62.8 s. We can see from these signals that the values of period vary from time to time between two crests.

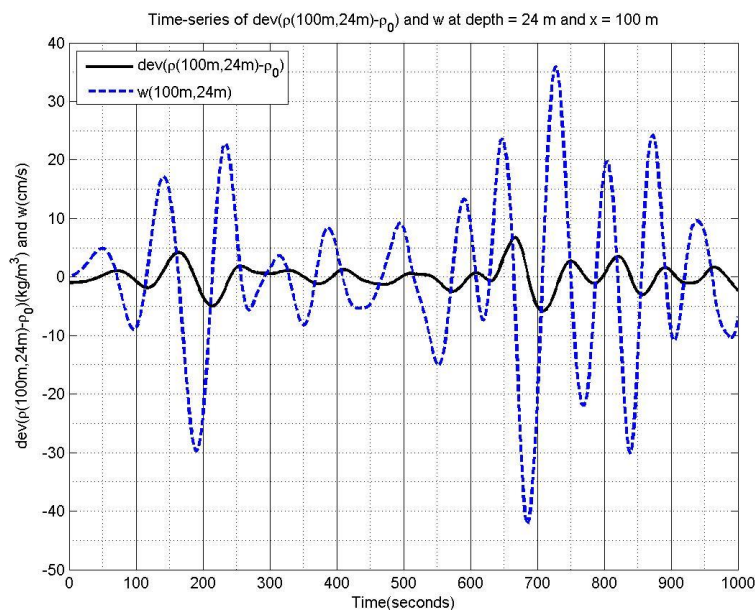


Fig. 4. Time-series of deviation of $(\rho - \rho_0)$ from its mean value in kg/m^3 (continuous line) and time-series of vertical velocity w in cm/s (dashed line). These lines are obtained at $x = 100$ m, and depth = 24 m.

The values of vertical velocity reach its maximum negative value at $w = -42.29$ cm/s and time = 687 s. While its maximum positive value reach its crest at $w = 35.93$ cm/s and time = 728 s.

Standing waves are formed from these two signals. They have a phase difference of $T/4$. From these lines, it can be seen that the turning points (maximum or minimum values) of $\text{dev}(\rho - \rho_0)$ is associated with vertical velocity at $w = 0$. It means the time function of $\text{dev}(\rho - \rho_0)$ and time function of w behave like a function and its derivative, respectively.

Figure 5 also shows the time-series of $\text{dev}(\rho - \rho_0)$ and vertical velocity w at $x = 100$ m and depth = 50 m. In general, it is shown that $\text{dev}(\rho - \rho_0)$ has greater values than that of depth = 24 m. The maximum and minimum values of vertical velocity also have higher values compared to those of depth = 24 m.

As shown in Fig. 4, Fig. 5 also confirms that the turning points of $\text{dev}(\rho - \rho_0)$ are associated with vertical velocity at $w = 0$ and there is also phase difference of $T/4$ between the line of $\text{dev}(\rho - \rho_0)$ and the line of vertical velocity w .

Figure 6 also shows the time-series of $\text{dev}(\rho - \rho_0)$ and vertical velocity w at $x = 100$ m and depth = 76 m. This figure also confirms that the turning points of $\text{dev}(\rho - \rho_0)$ correspond very good with vertical velocity at $w = 0$ and there is also phase difference of $T/4$ between the line of $\text{dev}(\rho - \rho_0)$ and the line of vertical velocity w .

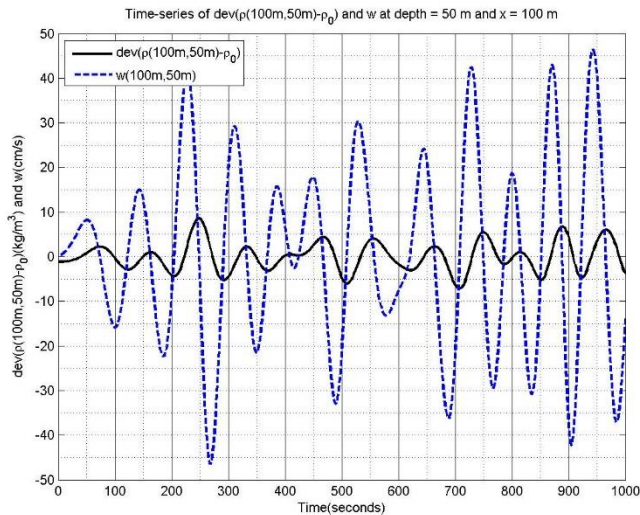


Fig. 5. Same as Fig. 4 but for $x = 100$ m, and depth = 50 m.

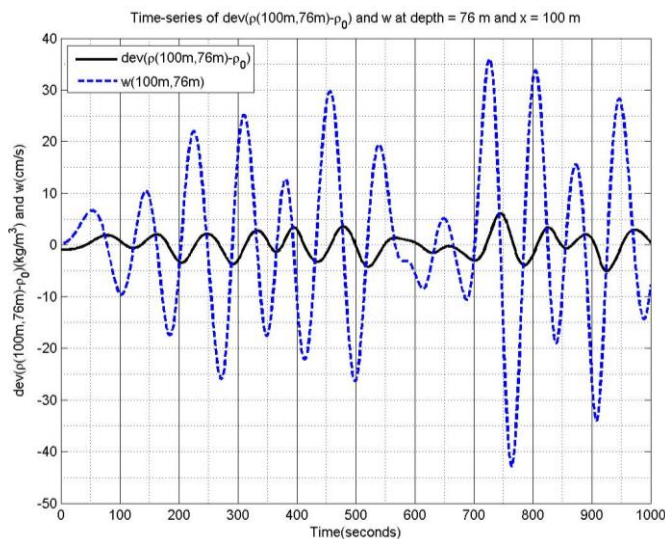


Fig. 6. Same as Fig. 4 but for $x = 100$ m, and depth = 76 m.

Figure 7 shows the circulation of the internal waves and $(\rho - \rho_0)$ at time-simulation of 800 s. It is shown that both circulation and $(\rho - \rho_0)$ are symmetric to the line $x = 250$ m. It can be understood since five cells in the middle of the channel have been used to force the internal waves (see Fig. 1).

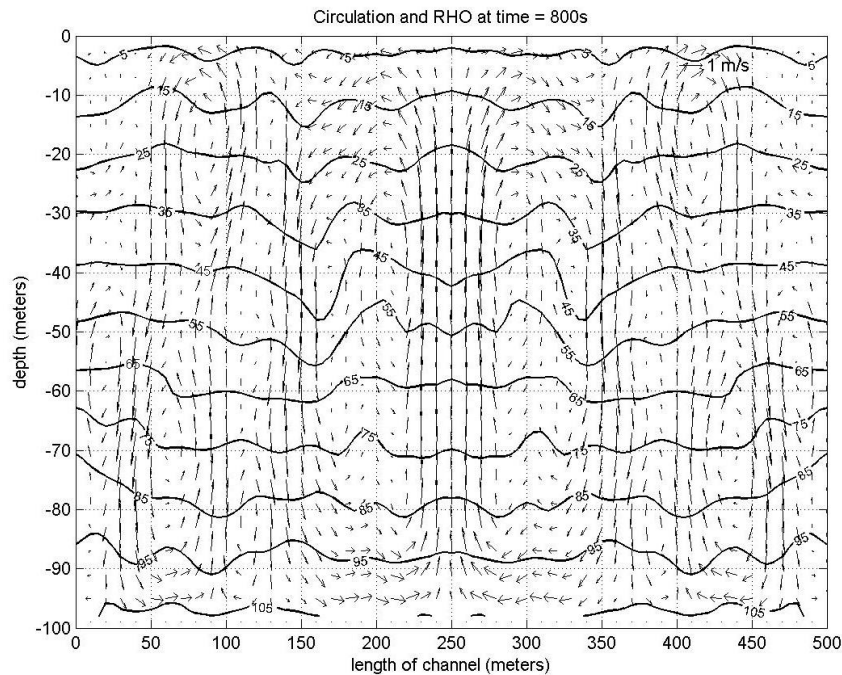


Fig. 7. Circulation and contour line of $(\rho - \rho_0)$ in kg/m^3 in xz -plane at time-simulation $t = 800$ s. In the x -axis and y -axis are the length of channel and depth in meters, respectively. Density at surface $\rho_0 = 1028 \text{ kg/m}^3$.

The line pattern of $(\rho - \rho_0)$ and circulation pattern are very complex. The line of $(\rho - \rho_0)$ increases with the depth. Near the surface, the value $(\rho - \rho_0)$ is 5 kg/m^3 or at $\rho = 1033 \text{ kg/m}^3$, since $\rho_0 = 1028 \text{ kg/m}^3$. The value of $(\rho - \rho_0)$ is 105 kg/m^3 , close to the bottom. Between $x = 250$ m and 375 m, the circulation pattern has a clockwise rotation from the surface to the bottom layer. Between $x = 375$ m and $x = 475$ m, the pattern has a clockwise rotation but this pattern has two groups.

The first group is observed between the surface layer and at depth = 50 m. The second group exists from depth = 50 m to the bottom layer. Between $x = 475$ m and 500 m, another one can still be detected where there is a pattern with clockwise rotation in depth between 30 and 90 m.

Figure 8 shows the circulation of the internal waves and contour lines of $(\rho - \rho_0)$ at time-simulation $t = 900$ s. Between $x = 250$ m and 300 m, the circulation pattern has a clockwise rotation from the surface to the depth of 40 m. From depths of 40 until 60 m, the pattern has an anticlockwise rotation. Between $x = 300$ m and 500 m, the circulation pattern has several groups. However, all of the groups have a similar anticlockwise rotation.

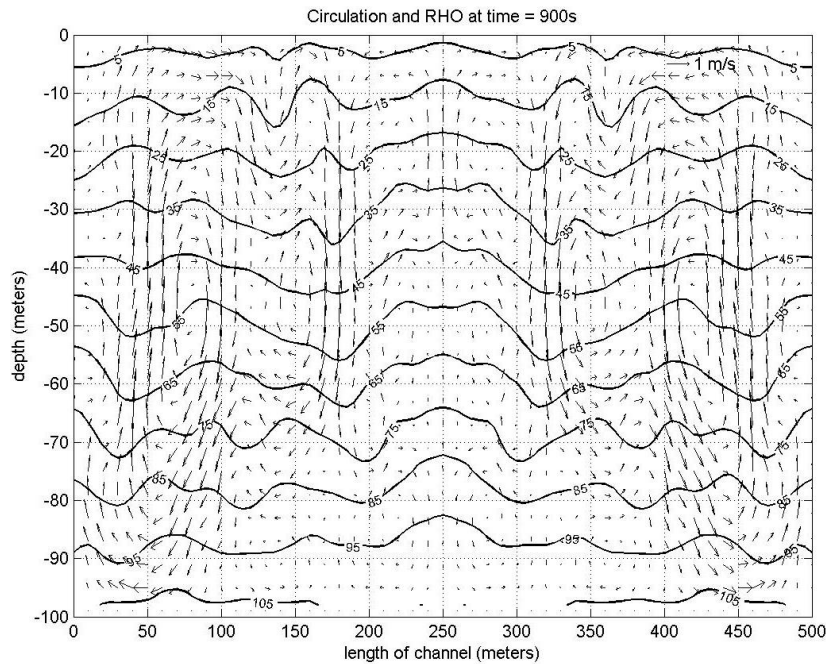


Fig. 8. Same as Fig. 7 but for time-simulation $t = 900$ s.

4. Conclusions

The simulation of internal waves in the area of constant topography with a depth of 500 meters, $dx = 5$ meters and $dz = 2$ meters, has been successfully carried out. The initial force is created with $N = 0.01$; it means the density is set up with increasing depth according to the value of $N = 0.01$. At the surface, the density is set up with the value of $\rho_0 = 1028.0 \text{ kg/m}^3$. Also, five cells in the middle (or $x = 250$ meters), the densities are added with the value of 20 kg/m^3 . Since this input data, the result will be symmetry about the line $x = 250$ m.

The signal of time-series at $x = 100$ m has 12 crests, and that of at $x = 200$ m has 14 crests. It means, compared to time-series at $x = 100$ m, the signal of time-series at $x = 200$ m has a smaller average period.

It is shown that both of lines of $\text{dev}(\rho - \rho_0)$ and vertical velocity w have 12 crests in 1000 s. It means they have average periods of $1000/12 = 83.3$ s. The minimum period is $2\pi/N = 62.8$ s. It is observed from these signals that the value of period varies from time to time between two crests.

The signals of $\text{dev}(\rho - \rho_0)$ and vertical velocity w form the standing waves. However, from these lines, we can still trace that the turning points (maximum or minimum values) of $\text{dev}(\rho - \rho_0)$ correspond with vertical velocity at $w = 0$. It means, there is a phase difference about $T/4$ between these waves. This difference is a very interesting finding because if both amplitudes have the same values, we can conclude that this is a system of a simple pendulum.

The line pattern of $(\rho - \rho_0)$ and circulation pattern are very complex for time-simulation of $t = 800$ s and 900 s. The clockwise or anticlockwise pattern is

observed from the circulation pattern. Because of the disturbance in the middle of the channel, $(\rho - \rho_0)$ and circulation pattern results in a symmetric form to the line x of 250 m.

We recommend conducting further research by adding tidal force as input in this study. Thus, the simulated waters will be more dynamic. In addition, the study of sediment transport in this domain is also quite interesting, because of the rapid vertical speed due to internal wave.

Acknowledgement

This research is funded by Universitas Syiah Kuala, Ministry of Research, Technology and Higher Education under the scheme of H-Index, with the contract number: 1712/UN11/SP/PNPB/2016.

Nomenclatures

| | |
|-------|---|
| g | Acceleration of gravity, m/s^2 |
| N^2 | Brunt-Väisälä frequency |
| P | Dynamic pressure, N/m^2 |
| U | Horizontal velocity, m/s |
| w | Vertical velocity, m/s |

Greek Symbols

| | |
|----------------------|--|
| Δt | Time-step, s |
| $\Delta x, \Delta z$ | Distance spacing in horizontal and vertical, respectively, m |
| ρ_0 | Constant reference density at the surface, 1028 kg/m^3 |
| ρ' | Density fluctuation, kg/m^3 |
| $\bar{\rho}$ | Depth-variable part of density, kg/m^3 |

References

- van der Lee, E.M.; and Umlauf, L. (2011). Internal wave mixing in the Baltic Sea: Near-inertial waves in the absence of tides. *Journal of Geophysical Research*, 116(C10), 1-16.
- Gavrilov, N.; Liapidevskii, V.; and Gavrilova, K. (2011). Large amplitude internal solitary waves over a shelf. *Natural Hazards and Earth System Sciences*, 11(1), 17-25.
- Guo, C.; and Chen, X. (2012). Numerical investigation of large amplitude second mode internal solitary waves over a slope-shelf topography. *Ocean Modelling*, 42, 80-91
- Lien, R.-C.; Henyey, F.; Ma, B.; and Yang, Y.J. (2014). Large-amplitude internal solitary waves observed in the Northern South China Sea: Properties and energetics. *Journal of Physical Oceanography*, 44(4), 1095-1115.
- Jochum, M.; Briegleb, B.P.; Danabasoglu, G.; Large, W.G.; Norton, N.J.; Jayne, S.R.; Alford, M.H.; and Bryan, F.O. (2013). The impact of oceanic near-inertial waves on climate. *Journal of Climate*, 26(9), 2833-2844.
- Alford, M.H.; Peacock, T.; MacKinnon, J.A.; Nash, J.D.; Buijsman, M.C.; Centuroni, L.R.; Chao, S.-Y.; Chang, M.-H.; Farmer, D.M.; Fringer, O.B.; Fu, K.-H.; Gallacher, P.C.; Graber, H.C.; Helfrich, K.R.; Jachec, S.M.; Jackson,

- C.R.; Klymak, J.M.; Ko, D.S.; Jan, S.; Johnson, T.M.S.; Legg, S.; Lee, I.-H.; Lien, R.-C.; Mercier, M.J.; Moum, J.N.; Musgrave, R.; Park, J.-H.; Pickering, A.I.; Pinkel, R.; Rainville, L.; Ramp, S.R.; Rudnick, D.L.; Sarkar, S.; Scotti, A.; Simmons, H.L.; St. Laurent, L.C.; Venayagamoorthy, S.K.; Wang, Y.-H.; Wang, J.; Yang, Y.J.; Paluszkiwicz, T.; and Tang, T.-Y. (2015). The formation and fate of internal waves in the South China Sea. *Nature*, 521(7550), 65-69.
7. DeCarlo, T.M.; Karauskas, K.B.; Davis, K.A.; and Wong, G.T.F. (2015). Climate modulates internal wave activity in the Northern South China Sea. *Geophysical Research Letters*, 42(3), 831-838.
 8. Chen, Z.-W.; Xie, J.; Wang, D.; Zhan, J.-M.; Xu, J.; and Cai, S. (2014). Density stratification influences on generation of different modes internal solitary waves. *Journal of Geophysical Research: Oceans*, 119(10), 7029-7046.
 9. Palmer, M.R.; Stephenson, G.R.; Inall, M.E.; Balfour, C.; Düsterhus, A.; and Green, J.A. M. (2015). Turbulence and mixing by internal waves in the Celtic Sea determined from ocean glider microstructure measurements. *Journal of Marine Systems*, 144, 57-69.
 10. Craig, W.; Guyenne, P.; and Sulem, C. (2012). The surface signature of internal waves. *Journal of Fluid Mechanics*, 710, 277-303.
 11. Pineda, J. (1999). Circulation and larval distribution in internal tidal bore warm fronts. *Limnology Oceanography*, 44(6), 1400-1414.
 12. Walter, R.K.; Squibb, M.E.; Woodson, C.B.; Koseff, J.R.; and Monismith, S.G. (2014). Stratified turbulence in the nearshore coastal ocean: Dynamics and evolution in the presence of internal bores. *Journal of Geophysical Research: Oceans*, 119(12), 8709-8730.
 13. Menni, Y.; Azzi, A.; Zidani, C.; and Benyoucef, B. (2016). Numerical analysis of turbulent forced-convection flow in a channel with staggered L-shaped baffles. *Journal of New Technology and Materials*, 6(2), 44-55.
 14. Menni, Y.; Azzi, A.; and Zidani, C. (2017). Use of waisted triangular-shaped baffles to enhance heat transfer in a constant temperature-surfaced rectangular channel. *Journal of Engineering Science and Technology (JESTEC)*, 12(12), 3251-3273.
 15. Menni, Y., and Azzi, A. (2018). Numerical analysis of thermal and aerodynamic fields in a channel with cascaded baffles. *Periodica Polytechnica Mechanical Engineering*, 62(1), 16-25.
 16. Menni, Y., and Azzi, A., (2018b). Computational fluid dynamical analysis of turbulent heat transfer in a channel fitted with staggered V-shaped baffles. *World Journal of Modelling and Simulation*, 14(2), 108-123.
 17. Walter, R.K.; Stastna, M.; Woodson, C.B.; and Monismith, S.G. (2016). Observations of nonlinear internal waves at a persistent coastal upwelling front. *Continental Shelf Research*, 117, 100-117.
 18. Mercier, M.J.; Gostiaux, L.; Helfrich, K.; Sommeria, J.; Viboud, S.; Didelle, H.; Ghaemsaïdi, S.J.; Dauxois, T.; and Peacock, T. (2013). Large-scale, realistic laboratory modeling of M2 internal tide generation at the Luzon Strait. *Geophysical Research Letters*, 40(21), 5704-5709.

19. Shanmugam, G. (2013). Modern internal waves and internal tides along oceanic pycnoclines: Challenges and implications for ancient deep-marine baroclinic sands. *AAPG Bulletin*, 97(5), 799-843.
20. Cheriton, O.M.; McPhee-Shaw, E.E.; Shaw, W.J.; Stanton, T.P.; Bellingham, J.G.; and Storlazzi, C.D. (2014). Suspended particulate layers and internal waves over the southern Monterey Bay continental shelf: An important control on shelf mud belts? *Journal of Geophysical Research Oceans*, 119(1), 428-444.
21. Matthews, J.P.; Aiki, H.; Masuda, S.; Awaji, T.; and Ishikawa, Y. (2011). Monsoon regulation of Lombok Strait internal waves. *Journal of Geophysical Research Oceans*, 116(C5), 1-14.
22. Salloum, M.; Knio, O.M.; and Brandt, A. (2012). Numerical simulation of mass transport in internal solitary waves. *Physics of Fluids*, 24(1), 016602.
23. Kämpf, J. (2010). *Advanced ocean modelling: Using open-source software*. Heidelberg, Germany: Springer-Verlag Berlin Heidelberg.
24. Rizal, S. (2000). The role of non-linear terms in the shallow water equation with the application in three-dimensional tidal model of the Malacca Strait and Taylor's problem in low geographical latitude. *Continental Shelf Research*, 20(15), 1965-1991.
25. Rizal, S. (2002). Taylor's problem - Influences on the spatial distribution of real and virtual amphidromes. *Continental Shelf Research*, 22(15), 2147-2158.
26. Rizal, S.; Setiawan, I.; Iskandar, T.; Ilhamsyah, Y.; Wahid, M.A.; and Musman, M. (2010). Currents simulation in the Malacca straits by using three-dimensional numerical model. *Sains Malaysiana*, 39(4), 519-524.
27. Rizal, S.; Damm, P.; Wahid, M.A.; Sündermann, J.; Ilhamsyah, Y.; Iskandar, T.; and Muhammad. (2012). General circulation in the Malacca Strait and Andaman Sea: A numerical model study. *American Journal of Environmental Sciences*, 8(5), 479-488.
28. Pond, S.; and Pickard, G.L. (1983). *Introductory Dynamical Oceanography* (2nd ed.). Houston, Texas, United States of America: Gulf Professional Publishing.